A simple predictive model for the eddy propagation trajectory in the northern South China Sea

Jiaxun Li[1,2], Guihua Wang[*1], Huijie Xue[3,4], and Huizan Wang[5]

[1]Department of Atmospheric and Oceanic Sciences, Institute of Atmospheric Science, Fudan University, Shanghai, China

[2]Naval Institute of Hydrographic Surveying and Charting, Tianjin, China

[3]State Key Laboratory of Tropical Oceanography, South China Sea Institute of Oceanology, Chinese Academy of Sciences, Guangzhou, China

[4]School of Marine Sciences, University of Maine, Orono, Maine, USA

[5]Institute of Meteorology and Oceanography, National University of Defense Technology, Nanjing, China

Corresponding author: Guihua Wang, Department of Atmospheric and Oceanic Sciences, Institute of Atmospheric Science, Fudan University, Shanghai, China. (wghocean@yahoo.com)

Abstract A novel predictive model is built for eddy propagation trajectory using the multiple linear regression method. This simple model has related various oceanic parameters to eddy propagation position changes in the northern South China Sea (NSCS). These oceanic parameters mainly represent the effects of β and mean flow advection on the eddy propagation. The performance of the proposed model is examined in the NSCS based on twenty years of satellite altimeter data, and demonstrates its significant forecast skills over a 4-week forecast window comparing to the traditional persistence method. It is also found that the model forecast accuracy is sensitive to eddy polarity and forecast season.

1. Introduction

Mesoscale eddies are coherent rotating structures that are ubiquitous over most of the world's oceans (Chelton et al., 2007). They play an important role in the transport of momentum, heat, mass and chemical and biological tracers, thereby become critical for issues such as general circulation, water mass distribution, ocean biology and climate change (Wang et al., 2012; Dong et al., 2014; Zhang et al., 2014; Ma et al., 2016; Li et al., 2017). Therefore, forecasting the eddy propagation positions accurately is not only important scientifically but also important practically for problems such as ocean observing systems designing, fishing planning, and underwater acoustic detecting.

Traditionally, ocean dynamical models were used as the tool of predicting the evolution of ocean eddies (Robinson et al., 1984). Since mesoscale eddies are often associated with strong nonlinear processes and their dynamical mechanisms are quite different, the operational forecast of eddies has been a big challenge to ocean numerical model. Much progress has been made in recent years in eddy-resolving ocean prediction. With the data assimilation and the increasing of model resolution, the model increases forecast skill. Daily forecast errors of eddy center positions in the northwestern Arabian Sea and Gulf of Oman are 44-68 km in $1/12^{o}$ global HYCOM model, and reach to 22.5-37 km in $1/32^{o}$ NLOM model (Hurlburt et al., 2008). The forecast skill and predictability of dynamical models can only be increased by better assimilation schemes (initialization), sufficient data (especially the subsurface), and improving resolution (physics and computing) (Rienecker et al., 1987; Oey et al., 2005). These restrictions preclude the all-pervading operational use of dynamical models when these initial data and computing power are not feasible due to some reasons.

In this paper, we developed a simple statistical model to predict the eddy positions 1-4 weeks in advance using only the past positions of the eddy and its surrounding fields.

Our “test block” of ocean is the northern South China Sea (NSCS). South China Sea is a semi-enclosed sea under the dramatic influence of the East Asian Monsoon and Kuroshio intrusion (Liu and Xie, 1999; Shaw, 1991). Due to the variable external forcing and complex topography, mesoscale eddies show obvious geographic distributions and various characteristics (Wang et al., 2003; Xiu et al., 2010; Chen et al., 2011), but the common character is the overall westward tendency of eddy trajectories no matter of the eddy polarity (Fig. 1). We will first analyze the pattern and dynamics of the common westward movement of eddies in the NSCS, then choose the potential predictors and develop a simple predictive model for eddy propagation trajectories, and finally evaluate the model performance and discuss the impact of eddy polarity and season on the forecast accuracy.

2. Data and Methods

2.1 Data

The sea level anomalies (SLA) are from the Archiving, Validation and Interpretation of Satellite Oceanographic data (AVISO, ftp://ftp.aviso.oceanobs.com/) (Ducet et al., 2000). The product merges the measurements of TOPEX/Poseidon, European Remote Sensing Satellite (ERS-1/2), Geosat Follow-on, Jason-1/2, and Envisat, and spans the period from October 14, 1992 to August 7, 2013. Its temporal resolution is weekly, and its spatial resolution is 0.25^{o} latitude by 0.25^{o} longitude. To estimate the large-scale geostrophic currents, we use the absolute dynamic topography (ADT), which consists of the SLAs and a mean dynamic topography (MDT). The method for calculating the MDT was introduced by Rio and Hernandez (2004), and the data is also distributed by AVISO.

The monthly climatology of observed ocean temperature and salinity from U.S. Navy Generalized Digital Environment Model (GDEM-Version 3.0) is used to calculate the phase speed of nondispersive baroclinic Rossby waves in the NSCS. It has a horizontal resolution of 0.25^{o} latitude by 0.25^{o} longitude, and 78 standard depths from

0 to 6600 m with the vertical resolution varying from 2 m at the surface to 200 m below 1600 m (Canes, 2009).

The NSCS eddy trajectory data is derived from the 3rd release of the global eddy dataset (http://cioss.coas.oregonstate.edu/eddies/). The eddy center positions within their trajectories are recorded at 7-day time intervals. A detailed description of the eddy trajectory dataset can be found in Chelton et al. (2011). To forecast the eddy trajectory 1-4 weeks in advance using the last position of the eddy, only eddies with a lifetime of 5 weeks or longer are retained in this study.

2.2 The Maximum Cross-Correlation Method

The maximum cross-correlation (MCC) method is a space-time lagged technique, which can estimate the surface motions from time-sequential remote sensing images. It has been successfully used to track clouds from geosynchronous satellite data (Leese et al., 1971), to compute sea-ice motion (Ninnis et al., 1986) and advective surface velocities (Emery et al., 1986) from sequential infrared satellite images, and to determine the propagation velocities of ocean eddies from satellite altimeter data (Fu, 2006, 2009). The MCC method used in this study is the same as that of Fu (2009), which is a little different with that of Emery et al. (1986). In the method of Emery et al., the correlations of the image in the subwindow with all the neighboring ones in the whole window at the next time are computed, and the speed and direction of the maximum correlation can be estimated. While in the method of Fu et al., the correlations of the SLA at a given location with all the neighboring SLA at various time lags are computed, and the speed and direction of the maximum correlation can be estimated. The reason of their difference may be due to the low time-space resolution of SLA comparing with other infrared satellite images.

The MCC method mainly consists of two procedures (Fu, 2009): first, the cross-correlations of the SLA time series (h) with others within a certain range box are computed for some time lags (ΔT) in multiples of 7 days (time resolution of SLA

data) at each grid node location (x, y) as:

$$C_{x,y}(\Delta x, \Delta y, \Delta T) = \overline{h(x, y, t)h(x+\Delta x, y+\Delta y, t+\Delta T)} \quad (1)$$

where Δx and Δy are the spatial lags and the over bar means time averaging. Second, the position of the maximum correlation at each time lag (ΔT) is identified and a speed can be derived from the time lag and the distance of this position from the origin. Then an average speed vector (u, v) weighted by the correlation coefficients is calculated from the estimates at various time lags as:

$$(u, v) = \frac{\sum_i (\Delta x_i / \Delta T_i, \Delta y_i / \Delta T_i) C_i}{\sum_i C_i} \quad (2)$$

where C_i is the maximum correlation at ΔT_i, and Δx_i, Δy_i are the distances between the position of maximum correlation and the origin. The average velocities are then assigned to the eddy movement velocities at the given grid point.

To focus on the global mesoscale eddy, the time lags were limited to less than 70 days and the dimension of the window was less than 400 km (Fu, 2009). While in the NSCS, the time lags should be limited to less than 42 days, since many correlation coefficients are below the 95% confidence level at larger time lags (Zhuang et al., 2010). Besides, Chen et al. (2011) found that eddies propagate with 5.0-9.0 cm/s in the NSCS. Thus the search radius can be generally limited as 300 km (9.0 cm/s*42 days $\approx$ 300 km) to reduce incidence of spurious MCC vectors. Since the mean flow and associated eddy propagation in the SCS have seasonal variability, we divided the weekly SLA data from 1992 to 2013 into four groups according to four seasons (winter: December-February, spring: March-May, summer: June-August, autumn: Septermber-November). Then the seasonal climatological eddy propagation velocities can be estimated from the same seasonal group at intervals of 1 week using the MCC method.

2.3 The Multiple Linear Regression Model

To develop a simple statistical predictive model for relating various oceanic parameters to eddy propagation position changes, the multiple linear regression method is used for developing such statistical forecast model. The multiple linear

144 regression is a linear approach to modeling the relationship between the response and
145 explanatory variables. This classical method has many practical uses in oceanography
146 and meteorology, such as the prediction of Arctic sea ice extent (Zhang, 2015), the
147 estimation of subsurface salinity profile (Bao et al, 2019), the estimation of
148 anthropogenic CO_2 accumulation in the Southern Ocean (Matear and McNeil, 2003),
149 the forecast of typhoon track (Aberson and Sampson, 2003) and intensity (Demaria
150 and Kaplan, 1994), Maddan-Julian Oscillation forecast (Seo, 2008), and ENSO
151 prediction (Dominiak and Terray, 2005).
152
153 In this study, the predictands (dependent variables) are the zonal and meridional
154 displacements at each forecast time from the initial position (Table 1). The choice of
155 the predictors based on physical analysis will be shown in detail in Section 3. Since
156 the variables used for the regression involve different scales and units, it is
157 inappropriate to use them directly, as it may cause the fitting to deviate from the
158 physical constraints. Thus all the variables are normalized with their anomalies
159 divided by their corresponding standard deviations before the regressing. After that,
160 the normalized predicted zonal (meridional) displacement *DX* (*DY*) can be estimated
161 using a multiple linear regression method:

162 $$DX_j = \sum_{i=1}^{n} a_{i,j} P_{i,} \quad j = 1, 4 \tag{3}$$

163 $$DY_j = \sum_{i=1}^{n} b_{i,j} P_{i,} \quad j = 1, 4 \tag{4}$$

164 where the subscript *j* refers to the forecast interval (1-4 weeks), the subscript *i* refers
165 to the serial number of normalized predictors (*P*), n represents the number of selected
166 predictors; *a* and *b* donate the regression coefficients of predictors onto *DX* and *DY*,
167 respectively.
168
169 There are a total of 8 regression equations, i.e., both the meridional and zonal
170 directions for the weeks of 1-4. We separate the whole eddy trajectories into two sets:
171 one for regressing and the other for forecasting. At week-1, we used 1981 (76%) eddy

trajectory segments (a segment is the distance between two neighboring eddy center positions at 7-day interval on a single eddy trajectory) of 283 eddy trajectories during 1992-2008 for regressing, and 623 (24%) eddy trajectory segments of 81 eddy trajectories during 2009-2013 for forecasting. The other forecast experiments for 2, 3, and 4 weeks maintain the same periods for regressing and forecasting. To evaluate the overall forecast ability of the model, the mean forecast error is defined as the averaged distance (D) between the predicted eddy positions and the satellite observed eddy positions following great circle distance (Ali et al., 2007):

$$D = R \bullet \arccos[\sin Y_o \sin Y_F + \cos Y_o \cos Y_F \cos(X_o - X_F)] \quad (5)$$

where R is the earth radius, X_o (X_F) and Y_o (Y_F) represent the observed (predicted) longitude and latitude in degrees, respectively.

3. Dynamics of Eddy Propagation in the NSCS and Choice of Predictors

3.1 Pattern and Dynamical Analysis of Eddy Propagation in the NSCS

One of the most important steps in the development of a regression model is the choice of independent variables (predictors). In choosing the potential predictors, the candidates should have a physical link (direct or indirect) with the eddy propagation. To investigate the dynamical factors associated with eddy propagation in the NSCS, the pattern of eddy propagation speeds should be estimated firstly.

Instead of a Lagrangian description of the movement of individual eddies as reported in the previous studies (e.g., Wang et al., 2003; Chen et al., 2011), the space-time lagged MCC method provides an Eulerian description of the pattern of eddy propagation speeds (Fu, 2009). As shown in Fig. 2a and 2d, the MCC method has mapped the propagation speeds of eddies in the NSCS for the winter and summer season, respectively. The propagation of eddies is generally westward in the ocean

interior and southward in the western boundary with the typical speed of 4-10 cm/s. The propagation direction of eddies generated southwest of Taiwan is southwestward along the 200-2000 m isobaths, indicating the steering effects of the ocean's bathymetry. There are two distinct differences between the winter season and the summer season: one is that the eddy propagation speed in winter is relatively larger than that in summer; and the other is that the influence of the western boundary current can be clearly seen near 16^{o}N-18^{o}N along the Vietnam coast in winter, creating an organized band of southward eddy propagation pattern, while this cannot be found in summer. The different patterns of the eddy propagation speed in winter and summer have revealed several details of the mean flow in the SCS: the large-scale circulation under the influence of northeasterly winter monsoon is stronger than that in the southwesterly summer monsoon, and the robust western boundary current in winter becomes relatively weak and unorganized in summer.

Eddies also have their own westward drift under the planetary β effect in the absence of any mean flow (Nof, 1981, Cushiman-Roisin, 1994). Their propagation speed is approximately the phase speed of the first baroclinic Rossby waves with preferences for small poleward and equatorward deflection of cyclonic and anticyclonic eddies in the global ocean, respectively (Chelton et al., 2007). Theoretically, the phase speed of the first baroclinic Rossby wave is $C_{R1} = -\beta R_1$, where the first baroclinic Rossby radius of deformation R_1 is estimated using the climatological GDEM temperature and salinity data. Figure 2b (2e) shows the theoretical phase speed of nondispersive baroclinic Rossby waves calculated from GDEM winter (summer) climatological temperature and salinity data. The direction of the phase speed is due west and the magnitude increases from about 2 cm/s in the north latitude to 12 cm/s in the south latitude. It should be noted that the difference between the winter and summer distributions of the phase speed of the first baroclinic Rossby wave is relatively small. The underlying reason is that the variation of

seasonal stratification in the upper layer has little effect on the seasonal distribution of the first baroclinic Rossby deformation radius (Chelton et al, 1998, Cai et al., 2008).

The differences between the satellite observed propagation speed (Fig. 2a and 2d) and the propagation speed induced by the β effect (Fig. 2b and 2e) in winter and summer are shown in Fig. 2c and 2f, respectively, which may represent the propagation speed caused by the advection of mean flow. To further illustrate the advection effect of mean flow, the winter (summer) mean dynamic topography is superimposed on the propagation speed caused by the mean flow. As can be seen, there is a good spatial correlation (0.61 in the zonal direction and 0.52 in the meridional direction, both of which are significant at the 95% confidence level) between the cyclonic eddy propagation speed advected by the mean flow and the large scale surface cyclonic circulation in winter, both of which are centered northwest of the Luzon Island (Fig. 2c). Due to the weak cyclonic gyre in the NSCS, the spatial correspondence in summer is not as obvious as that in winter (Fig. 2f). Since the propagation speed induced by the β effect is westward, this tendency is reinforced by the mean flow in the north, but compensated by the mean flow in the south. Because the mean flow in the south is not so strong, it is not able to reverse eddy propagation from its westward motion induced by the β effect as in the Antarctic Circumpolar Current region (Klocker and Marshall, 2014) no matter in winter or summer.

To explore other possible causes of eddy propagation, Fig. 3a shows the annual mean eddy propagation speed. The most striking pattern is that the eddy propagation speed is accelerated markedly on the northern continental shelf of the NSCS (also can be seen in Fig. 2a and 2d), corresponding well to the region of negative maximum

meridional topographic $\beta_T = \frac{f}{H}\frac{dH}{dy}$, where H is the water depth. Their correlation is -0.40, which is significant at the 95% confidence level. This relatively good correspondence suggests that besides the planetary β effect and advection of mean flow, the topographic β effect also contributes to the eddy propagation in some regions where the bathymetry gradient cannot be neglected.

3.2 Choice of Predictors

As mentioned above, the mean flow advection and the effects of β (both planetary and topographic) are closely related with the eddy propagation. These factors should be considered as the potential predictors, and the seasonal climatological eddy zonal and meridional motions (U_CLIM V_CLIM) derived from the MCC are calculated to represent the effects of β and the mean flow advection. It is noted that we have tried to decompose U_CLIM and V_CLIM into the effects of β and the mean flow advection and incorporate them into the regression model, but found no improvement of the forecast skill.

In reality, the large-scale circulation evolves during the forecast period, this synoptic effect of mean flow advection should also be taken into account. To help account for the time variation of the mean flow advection, the current zonal and meridional absolute geostrophic flows (U_ADT, V_ADT) derived from the satellite data are evaluated at the beginning of the forecast time along the eddy trajectory. Besides, the persistence factors should also be considered in the regression model, since they contain the "latest" pattern of eddy propagation under the effects of β and the mean flow advection. The chosen persistence factors are the initial eddy position (LON, LAT) and the eddy motion past 1-week (U_PAST, V_PAST). All the chosen eight predictors are listed in Table 2, and can be derived along the eddy trajectories. They can be divided into two categories: 1) P1-P6 related to climatology and persistence,

i.e., “static predictors”, and 2) P7-P8 related to the changing environmental conditions, i.e., “synoptic predictors”.

The relative contribution of each predictor on each forecast period is illustrated by the normalized regression coefficient (Table 3). The larger the normalized regression coefficient, the greater its contribution to the individual forecast equation. Persistence factors (U_PAST, V_PAST) are initially the most important predictors, while after 2 weeks the most important predictors are the climatology factors (U_CLIM, V_CLIM). The synoptic predictors (U_ADT, V_ADT) contribute less to the forecast equations comparing with persistence and climatology. The underlying reason may be that the week to week variations are too large so the representation of the initial U_ADT and V_ADT to the actual velocities in the 4-week window is not as good as the U_CLIM and V_CLIM.

4. Performance of the Multiple Regression Model

4.1 Comparison with the persistence method

To evaluate the performance of our prediction model, the persistence method (no change of propagation speed from the initial state, Fig. 4a) and our model are used to predict the eddy trajectories during 2009-2013. Then the root-mean-square error (RMSE) and correlation coefficient between the predicted and actual longitudes (latitudes), and mean distance errors of our model and persistence method over a 4-week horizon are computed.

Table 4 lists the comparison of prediction results. It shows that our multiple linear regression model beats the persistence method and indicates our model has some forecast skill (Table 5): the RMSE between the predicted and the actual longitudes (latitudes) throughout the 4-week horizon is 32.7-89.2 km (29.5-73.5 km) with the correlation coefficients >0.93 (>0.95).

As an example, Fig. 5 compares the 1-2 weeks forecast performances of our model (blue) and the persistence method (green) with the observation (red). Generally, the eddy trajectory predicted 1-2 weeks in advance by our model coincides well with the observed trajectory with an overall average error of 27.6 km (week-1) and 42.5 km (week-2), and even the convoluted pattern can be reproduced properly (Fig. 5 (right)) though the mean error is slightly larger than the smooth case. In contrast, although the persistence forecast trajectory at week-1 is relatively consistent with the observation (Fig. 5a and 5b), the persistence method cannot forecast the eddy trajectories properly when the forecast horizon increases (Fig. 5c and 5d). To further compare their differences, their forecast distance errors are normalized with the Rossby radius on each forecast grid over 4-week forecast window, respectively. The correlation between the normalized forecast distance errors of the persistence method and our model decreases from 0.67 at week-1 to 0.38 at week-4. This is consistent with the above judgement and confirms the superiority of our multiple linear regression model over the persistence method.

4.2 Sensitive Performance of Different Eddy Polarity and Season

Previous studies have shown that anticycloinc eddies and cyclonic eddies in the NSCS have different dynamic characteristics, such as generation sites, rotation speeds and propagation trajectories, and the seasonal variability of these eddies is robust (Wang et al., 2006; Wang et al., 2008; Li et al., 2011). Two natural questions arise: 1) is there any difference on the model forecast ability between anticyclonic eddies (Fig. 1a) and cyclonic eddies (Fig. 1b)? 2) If so, is there any difference on the forecast ability for one type of eddies in winter (Fig. 7a and 8a) and summer (Fig. 7b and 8b)? This section will explore the different model performances on two types of eddies and during different seasons in the NSCS.

The period considered for regressing and predicting the anticyclonic eddy and cyclonic eddy positions is the same as that used in developing the predictive model in

Section 2.3. The mean forecast errors of anticyclonic (cyclonic) eddies from week-1 to week-4 are 36.9 km (41.1 km), 62.6 km (68.1 km), 81.0 km (88.5 km), and 102.0 km (108.2 km), respectively (Fig. 6). These results show that the forecast errors of anticyclonic eddies are smaller than those of cyclonic eddies in all forecast horizon, and the maximum error difference can reach 7.5 km at week-3. To investigate the underlying reasons of different model performances for anticyclonic eddies and cyclonic eddies, we use the persistence error ($CC' = \sqrt{AB^2 + BC^2 - 2AB \bullet BC \bullet \cos\theta}$ in Fig. 4a) at week-1 as an index to measure the difficulty of trajectory forecast. The underlying reason in physics is that CC', which includes the effects of winding angel (θ, measuring the trajectory curvature) and the eddy propagation distances in the former and latter periods (AB and BC, measuring the eddy propagation speed), is an integral characteristic of eddy trajectory. The correlation between this integrated index and eddy trajectory forecast error is relatively high with R=0.62 (Fig. 4b), which is significant at the 95% confidence level and shows its ability of measuring the inherent difficulty of trajectory forecast: the larger the index, the more difficult the trajectory forecast, thus the larger the forecast error. Because the indices (mean persistence errors) of all the anticyclonic and cyclonic eddy trajectories in the NSCS are 46.6 km and 53.0 km, respectively, it is not difficult to understand why the mean forecast error of anticyclonic eddy trajectories is smaller than that of cyclonic eddy trajectories in the NSCS. The index difference between anticyclonic and cyclonic eddy trajectories is caused by these different trajectory patterns (Fig. 1a and 1b), which could be due to the opposing meridional drifts of anticyclonic and cyclonic eddies expected from the combination of β effect and self-advection (Morrow et al., 2004).

Figure 7c (Fig. 8c) shows the mean forecast errors of anticyclonic (cyclonic) eddy trajectories in winter and summer over a 4-week horizon. Because the mean persistence error (42.0 km) of anticyclonic eddy trajectories in winter is smaller than that (51.9 km) in summer, as expected, the mean forecast error of anticyclonic eddy trajectories in winter is smaller than that in summer for all cases. This is also the case

for the cyclonic eddy: since the mean persistence error (54.6 km) of cyclonic eddy trajectories in winter is relatively larger than that (52.8 km) in summer, the mean forecast error of cyclonic eddy trajectories in winter is larger than that in summer. The index difference of one type of eddy trajectories between winter and summer is also caused by the different trajectory patterns. Why do the anticyclonic and cyclonic eddies follow different trajectories in winter (Fig. 7a and 8a) and summer (Fig. 7b and 7b)? One possible dynamical reason is the different interactions between the eddies and seasonal mean flows. Other underlying factors such as eddy generation mechanisms and eddy-topography interactions in different seasons may also contribute. This is beyond the scope of this study and needs further investigation using numerical models.

5. Summary and Discussion

In this study, we have investigated the underlying dynamics of the eddy propagation in the NSCS and found their propagation is mainly driven by the combination of the planetary β effect and mean flow advection. In addition, the topographic β effect also has some contribution to the eddy propagation where the bathymetry gradient cannot be neglected, like the steep continental shelf in the NSCS (Fig. 1a).

Based on the dynamical analysis, predictors are chosen and a simple statistical predictive model for relating various oceanic parameters to eddy propagation position changes is developed using the multiple linear regression method. This predictive model is made up of eight predictands (zonal and meridional displacements over 1-4 weeks) and eight predictors (six static predictors, two synoptic predictors). The six static predictors are associated with the initial position, the zonal and meridional motions past 1-week, and the climatological eddy zonal and meridional motions. The other two synoptic predictors account for the time variation of the mean flow advection. Results showed that this simple model has significant forecast skills over a

4-week forecast horizon comparing the traditional persistence method. Moreover, the model performance is sensitive to eddy type and forecast season: 1) the predicted trajectory errors of anticyclonic eddies are smaller than those of cyclonic eddies; 2) the predicted trajectory errors of anticyclonic eddies in winter are smaller than those in summer; while the contrary is the case for the cyclonic eddy. The predictive model performance strongly depends on the inherent difficulty of trajectory forecast.

Although the performance of the proposed predictive model is encouraging, it could be refined further. Further improvement may be possible by including the effect of eddy-eddy interactions on the eddy propagation, which is supposed to help induce the eddy trajectory curve or loop (Early et al., 2011). Another possible improvement is to use artificial neural network (ANN) in developing the forecast model. ANN has been successfully used in the predicting cyclone tracks (Ali et al., 2007) and loop current variation (Zeng et al, 2015). ANN can represent both linear and non-linear relationships learned directly from the data being modeled. It mainly contains three layers: the input layer, the hidden layer, and the output layer. To be consistent with the multiple linear regression model, both the input layer and the output layer include the same predictors and predictands as the regression model, respectively. The hidden layer consists of two layers of neural variables. Through iterations on backward propagation of the error, the neural network learns by itself to achieve an optimum weighting function and a minimum error. The forecast errors of ANN for 1-4 weeks are listed in Table 4. We can see that some improvements (0.3-4.2 km during 1-4 weeks forecast horizon) have been shown comparing with the linear regression method. Recently, Jiang et al. (2018) have found the deep learning algorithm of neural networks performs better than the simple ANN for the parameterization of typhoon-ocean feedback in typhoon forecast models. These enhancements (both physics and algorithms) are topics warranting future research and development.

Data availability. The SLA and MDT data can be downloaded from AVISO (ftp://ftp.aviso.oceanobs.com/), and the NSCS eddy trajectory data can be derived from the 3rd release global eddy dataset (http://cioss.coas.oregonstate.edu/eddies/).

Acknowledgements. This work is supported by the National Key Research and Development Program of China (2017YFC1404103), the National Basic Research Program of China (2013CB430301), the Natural Science Foundation of China (91428206, 41621064, 91528304), the National Programme on Global Change and Air-Sea Interaction (GASIIPOVAI-04), and the China Postdoctoral Science Foundation (2016M601493).

References

Aberson, S. D. and Sampson, C. R.: On the predictability of tropical cyclone tracks in the northwest pacific basin, Mon. Wea. Rev., 131, 1491-1497, 2003.

Ali, M. M., Kishtawal, C. M., and Jain, S.: Predicting cyclone tracks in the north Indian Ocean: An artificial neural network approach, Geophys. Res. Lett., 34, L04603, http://doi.org/10.1029/2006GL028353, 2007.

Bao, S., Zhang, R. Wang, H., Yan, H., and Yu, Y.: Salinity profile estimation in the Pacific Ocean from satellite Surface salinity observations, J. Atmos. Oceanic. Technol., 36, 53-68, 2019.

Cai, S., Long, X., Wu, R., and Wang, S.: Geographical and monthly variability of the first baroclinic rossby radius of deformation in the south china sea, J. Mar. Syst., 74, 711-720, 2008.

Canes, M. R.: Description and evaluation of GDEM-V3.0, Rep.NRL/MR/7330-09-9165, Nav. Res. Lab, Washington, D. C, 2009.

Chelton, D. B., Schlax, M. G., and Samelson, R. M.: Global observations of nonlinear mesoscale eddies, Prog. Oceanogr., 91, 167-216, 2011.

Chelton, D. B., Schlax, M. G., Samelson, R. M., and de Szoeke, R. A.: Global observations of large oceanic eddies, Geophys. Res. Lett., 34, L15606, http://doi.org/10.1029/2007GL030812, 2007.

446 Chelton, D., DeSzoeke, R., and Schlax, M.: Geographical variability of the first baroclinic rossby
447 radius of deformation, J. Phys. Oceanogr., 28, 433-460, 1998.
448 Chen, G., Hou, Y., and Chu, X.: Mesoscale eddies in the South China Sea: Mean properties,
449 spatiotemporal variability, and impact on thermohaline structure, J. Geophys. Res., 116, C06018,
450 http://doi.org/10.1029/2010JC006716, 2011.
451 Cushiman-Roisin, B.: Introduction to Geophysical Fluid Dynamics, Prentice Hall, 320 pp, 1994.
452 Demaria, M. and Kaplan, J.: A statistical hurricane intensity prediction scheme (SHIPS) for the
453 Atlantic basin, Weather Forecast, 9, 209-220, 1994.
454 Dominiak, S., and Terray, P.: Improvement of ENSO prediction using a linear regression model
455 with a southern Indian Ocean sea surface temperature predictor, Geophys. Res. Lett., 32,
456 L18702, doi:10.1029/2005GL023153, 2005.
457 Dong, C., Mcwilliams, J. C., Liu, Y., and Chen, D.: Global heat and salt transports by eddy
458 movement, Nature Communications, 5, 3294, 2014.
459 Ducet, N., Le Traon, P. Y., and Reverdin, G.: Global high-resolution mapping of ocean circulation
460 from TOPEX/Poseidon and ERS-1 and -2, J. Geophys. Res., 105, 19477–19498,
461 http://doi.org/10.1029/2000JC900063, 2000.
462 Early, J. J., Samelson, R. M., and Chelton, D. B.: The evolution and propagation of
463 quasigeostrophic ocean eddies, J. Phys. Oceanogr., 41, 1535-1555, 2011.
464 Emery, W. J., Thomas, A. C., Collins, M. J., Crawford, W. R., and Mackas, D. L.: An objective
465 method for computing advective surface velocities from sequential infrared satellite images, J.
466 Geophys. Res., 91, 12865–12878, http://doi.org/ 10.1029/JC091iC11p12865, 1986.
467 Fu, L.-L.: Pathways of eddies in the South Atlantic Ocean revealed from satellite altimeter
468 observations, Geophys. Res. Lett., 33, L14610, http://doi.org/10.1029/2006GL026245, 2006.
469 Fu, L.-L.: Pattern and speed of propagation of the global ocean eddy variability, J. Geophys.
470 Res., 114, C11017, http://doi.org/10.1029/2009JC005349, 2009.
471 Hurlburt, H., Chassignet, E., Cummings, J., Kara, A., Metzger, E., Shriver, J., Smedstad, O.,
472 Wallcraft, A., and Barron., C.: Eddy Resolving Global Ocean Prediction, Washington D. C.,
473 American Geophysical Union Geophysical Monograph Series, 353-381, 10.1029/177GM21,
474 2008.
475 Jiang, G.-Q., Xu, J., & Wei, J.: A deep learning algorithm of neural network for the

parameterization of typhoon-ocean feedback in typhoon forecast models, Geophys. Res. Lett., 45, https://doi.org/10.1002/2018GL077004, 2018.

Klocker, A. and Marshall, D. P.: Advection of baroclinic eddies by depth mean flow, Geophys. Res. Lett., 41, 3517–3521, http://doi.org/10.1002/2014GL060001, 2014.

Leese, J. A., Novak, C. S., and Clark, B. B.: An automated technique for obtaining cloud motion from geosynchronous satellite data using cross correlation, J. Appl. Meteor., 10, 18-132, 1971.

Li, J., Zhang, R., and Jin, B.: Eddy characteristics in the northern South China Sea as inferred from Lagrangian drifter data, Ocean Sci., 7, 1575-1599, 2011.

Li, J., Wang, G., and Zhai, X.: Observed cold filaments associated with mesoscale eddies in the South China Sea, J. Geophys. Res. Oceans, 122, 762–770, http://doi.org/10.1002/2016JC012353, 2017.

Liu, W. T. and Xie, X.: Space-based observations of the seasonal changes of South Asian monsoons and oceanic response, Geophys. Res. Lett., 26, 1473-1476, 1999.

Ma, X. and Coauthors: Western boundary currents regulated by interaction between ocean eddies and the atmosphere, Nature, 535, 533, 2016.

Matear, R. J., and McNeil, B. I.: Decadal accumulation of anthropogenic CO2 in the Southern Ocean: A comparison of CFC-age derived estimates to multiple-linear regression estimates, Global Biogeochem. Cycles, 17(4), 1113, doi:10.1029/ 2003GB002089, 2003.

Morrow, R., Birol, F., Griffin, D., and Sudre, J.: Divergent pathways of cyclonic and anti-cyclonic ocean eddies, Geophys. Res. Lett., 31, L24311, http://doi.org/10.1029/2004GL020974, 2004.

Ninnis, R. M., Emery, W. J., and Collins, M. J.: Automated extraction of pack ice motion from advanced very high resolution radiometer imagery, J. Geophys. Res., 91, 10725–10734, http://doi.org/10.1029/JC091iC09p10725, 1986.

Nof, D.: On the β-induced movement of isolated baroclinic eddies, J. Phys. Oceanogr., 11, 1662-1672, 1981.

Oey, L.-Y., Ezer, T., Forristall, G., Cooper, C., DiMarco, S., and Fan, S.: An exercise in forecasting loop current and eddy frontal positions in the Gulf of Mexico, Geophys. Res. Lett., 32, L12611, http://doi.org/10.1029/2005GL023253, 2005.

Rienecker, M. M., Mooers, C. N. K., and Robinson, A. R.: Dynamical interpolation and forecast of the evolution of mesoscale features off northern California, J. Phys. Oceanogr., 17, 1189-1213,

1987.

Rio, M.-H. and Hernandez, F.: A mean dynamic topography computed over the world ocean from altimetry, in situ measurements, and a geoid model, J. Geophys. Res., 109, C12032, http://doi.org/10.1029/2003JC002226, 2004.

Robinson, A. R., Carton, J. A., Mooers, C. N. K., Walstad, L. J., Carter, E. F., Rienecker, M. M., Smith, J. A., and Leslie, W. G.: A real-time dynamical forecast of ocean synoptic/mesoscale eddies, Nature, 309, 781-783, 1984.

Seo, K. H., Wang, W., Gottschalck, J., Zhang, Q., Schemm, J.-K., Higgins, W., and Kumar, A.: Evaluation of MJO Forecast Skill from Several Statistical and Dynamical Forecast Models, J Clim., 22(9), 2372-2388, 2009.

Shaw, P. T.: Seasonal variation of the intrusion of the Philippine Sea water into the South China Sea, J. Geophys. Res., 96, 821-827, 1991.

Wang, G., Chen, D., and Su, J.: Generation and life cycle of the dipole in the South China Sea summer circulation, J. Geophys. Res., 111, C06002, http://doi.org/10.1029/2005JC003314, 2006.

Wang, G., Chen, D., and Su, J.: Winter eddy genesis in the eastern South China Sea due to orographic wind-jets, J. Phys. Oceanogr., 38, 726–732, http://doi.org/10.1175/2007JPO3868.1, 2008.

Wang, G., Li, J., Wang, C., and Yan, Y.: Interactions among the winter monsoon, ocean eddy and ocean thermal front in the South China Sea, J. Geophys. Res., 117, C08002, http://doi.org/10.1029/2012JC008007, 2012.

Wang, G., Su, J., and Chu, P. C.: Mesoscale eddies in the South China Sea observed with altimeter data, Geophys. Res. Lett., 30, 2121, http://doi.org/10.1029/2003GL018532, 21, 2003.

Xiu, P., Chai F., Shi, L., Xue, H., and Chao, Y.: A census of eddy activities in the South China Sea during 1993–2007, J. Geophys. Res., 115, C03012, http://doi.org/10.1029/2009JC005657, 2010.

Zhang, R.: Meachanims for the low frequency of summer Arctic sea ice extent, Proc. Natl. Acad. Sci., 112(15), 4570-4575, 2015.

Zhang, Z., Wang, W., and Qiu, B.: Oceanic mass transport by mesoscale eddies, Science, 345, 322, 2014.

Zeng, X., Li, Y., and He, R.: Predictability of the loop current variation and eddy shedding process

in the Gulf of Mexico using an artificial neural network approach, J. Atmos. Oceanic. Technol., 32, 1098-1111, 2015.

Zhuang W., Du, Y., Wang, D., Xie, Q., and Xie, S.-P.: Pathways of mesoscale variability in the South China Sea, Chin. J. Oceanol. Limnol., 28, 1055-1067, 2010.

542 **Figure and Table Captions**

543 **Figure 1.** The trajectories of (a) anticyclonic and (b) cyclonic eddies with lifetime≥5
544 weeks in the northern South China Sea (SCS). The solid circle represents the ending
545 position of each trajectory. In Fig. 1a, TI: Taiwan Island, LI: Luzon Islands, VN:
546 Vietnam. The two isobaths are for 200 m and 2000 m, respectively.

547 **Figure 2.** Winter climatology of (a) eddy propagation speed directions (vectors) and
548 magnitudes (color, cm/s), (b) The phase speed directions (vectors) and magnitudes
549 (color, cm/s) of the first baroclinic Rossby wave. (c) The speed difference (vectors)
550 between (a) and (b) superimposed on the winter mean absolute dynamic topography
551 (color, cm). (d), (e) and (f) are the same as (a), (b) and (c), respectively, but for the
552 summer.

553 **Figure 3.** (a) Annual mean of eddy propagation speed directions (vectors) and
554 magnitudes (color, cm/s). (b) Meridional distribution of the topographic β effect
555 (color shading).

556 **Figure 4.** (a) Schematic of persistence method. A, B, and C are three observed eddy
557 positions on the trajectory every 1 week interval. C' is the predictive eddy position 1
558 week in advance by persistence method, that is BC'=AB. Thus CC' is the persistence
559 error at week-1. (b) Scatterplot of persistence error versus forecast error of our model
560 at week-1 with best fit linear regression.

561 **Figure 5.** A comparison of the satellite observed trajectory (red), the predicted
562 trajectory by our model (blue) and persistence trajectory (green) at (a) week-1, (c)
563 week-2. (b), (d) are the same as (a) and (c), respectively, but for a recurved trajectory.
564 The biweekly eddy positions on each trajectory are shown by the solid circles.

565 **Figure 6.** Comparison of the mean forecast errors between anticyclonic eddies (red)
566 and cyclonic eddies (blue) over a 4-week window.

567 **Figure 7.** The trajectories of anticyclonic eddies in (a) winter and (b) summer with
568 lifetime≥5 weeks in the northern South China Sea. The solid circle represents the

ending position of each trajectory. (c) Comparison of their mean forecast errors over a 4-week window.

Figure 8. The same as Fig. 6, but for the cyclonic eddies.

Table 1. The eight predictands used in the predictive model.

Table 2. The eight predictors used in the predictive model.

Table 3. Normalized regression coefficients $a_{i,j}$ ($b_{i,j}$) for use with the eddy zonal (meridional) motion prediction equation.

Table 4. Comparison of mean forecast distance errors (km) of the persistence, multiple linear regression (MLR), and artificial neural network (ANN) method.

Table 5. Statistics of our muliple linear regression model for different forecast time of eddy propagation positions in terms of longitudes (latitudes).

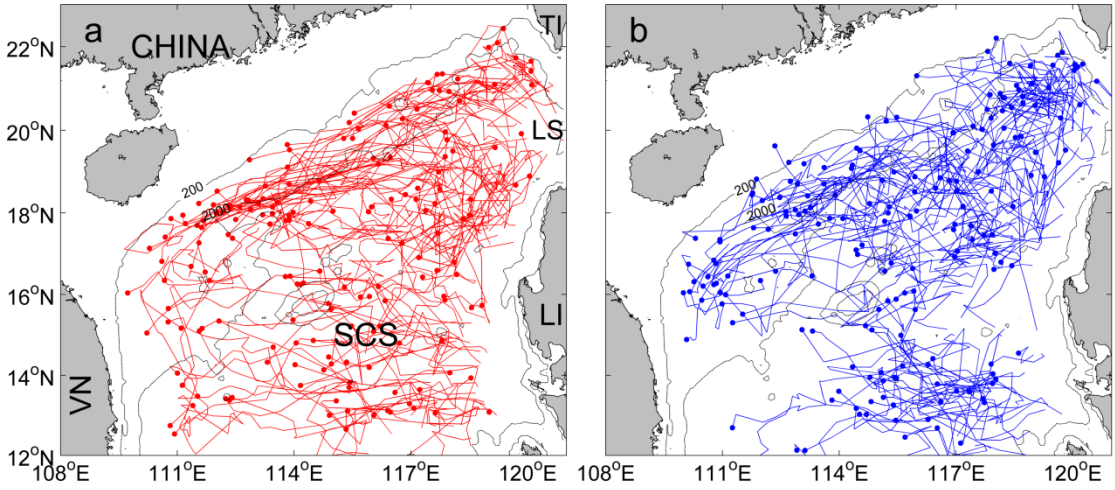

Figure 1. The trajectories of (a) anticyclonic and (b) cyclonic eddies with lifetime≥5 weeks in the northern South China Sea (SCS). The solid circle represents the ending position of each trajectory. In Fig. 1a, TI: Taiwan Island, LI: Luzon Islands, VN: Vietnam. The two isobaths are for 200 m and 2000 m, respectively.

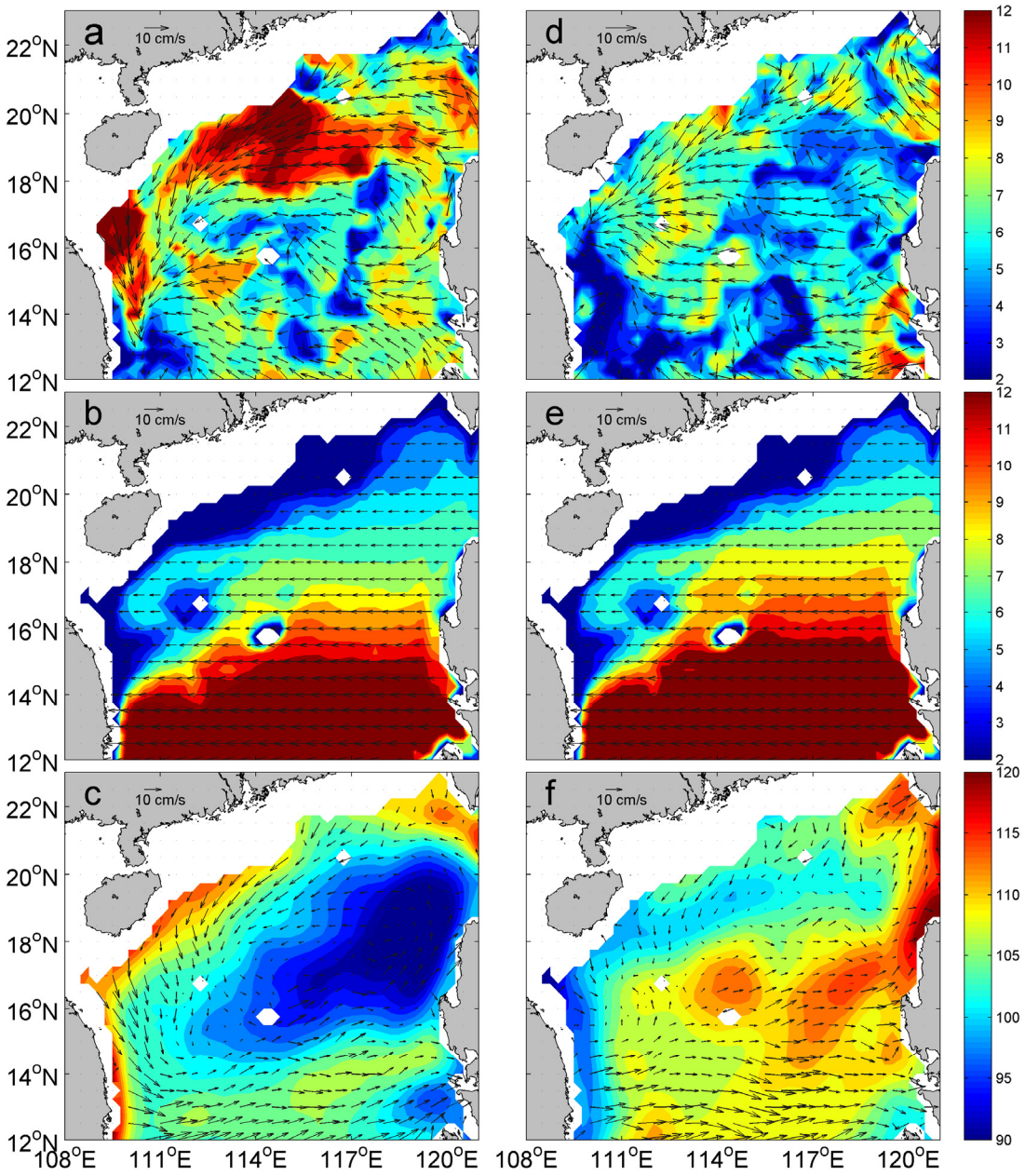

591

592

593 **Figure 2.** Winter climatology of (a) eddy propagation speed directions (vectors) and
594 magnitudes (color, cm/s), (b) The phase speed directions (vectors) and magnitudes
595 (color, cm/s) of the first baroclinic Rossby wave. (c) The speed difference (vectors)
596 between (a) and (b) superimposed on the winter mean absolute dynamic topography
597 (color, cm). (d), (e) and (f) are the same as (a), (b) and (c), respectively, but for the
598 summer.

599

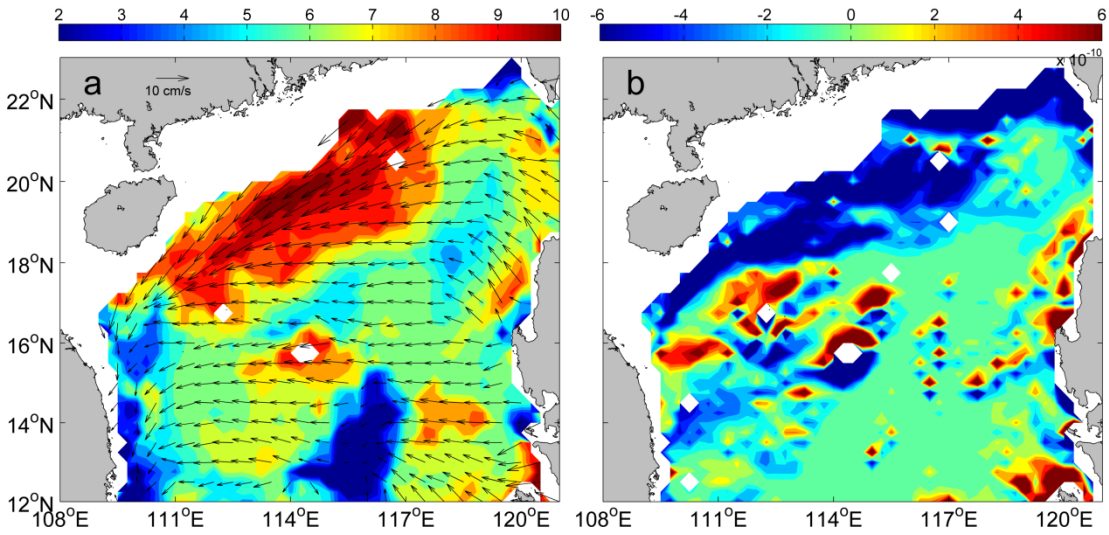

Figure 3. (a) Annual mean of eddy propagation speed directions (vectors) and magnitudes (color, cm/s). (b) Meridional distribution of the topographic β effect (color shading).

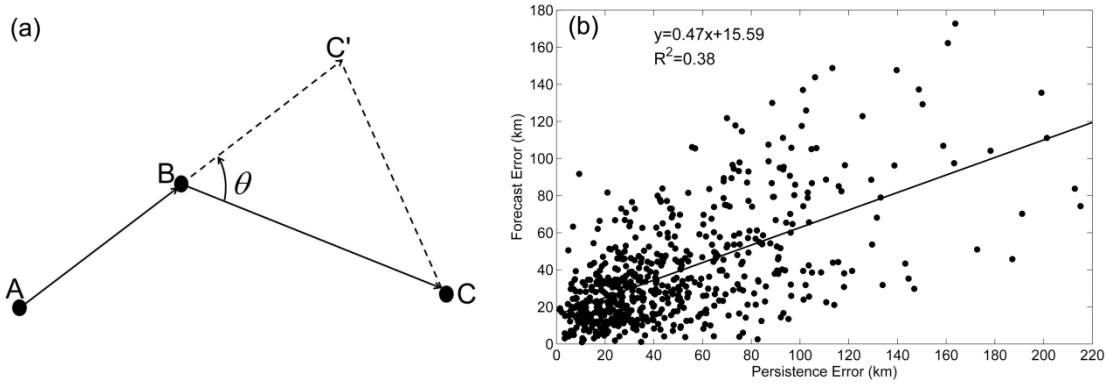

606

607

608 **Figure 4.** (a) Schematic of persistence method. A, B, and C are three observed eddy
609 positions on the trajectory every 1 week interval. C' is the predictive eddy position 1
610 week in advance by persistence method, that is BC'=AB. Thus CC' is the persistence
611 error at week-1. (b) Scatterplot of persistence error versus forecast error of our model
612 at week-1 with best fit linear regression.

613

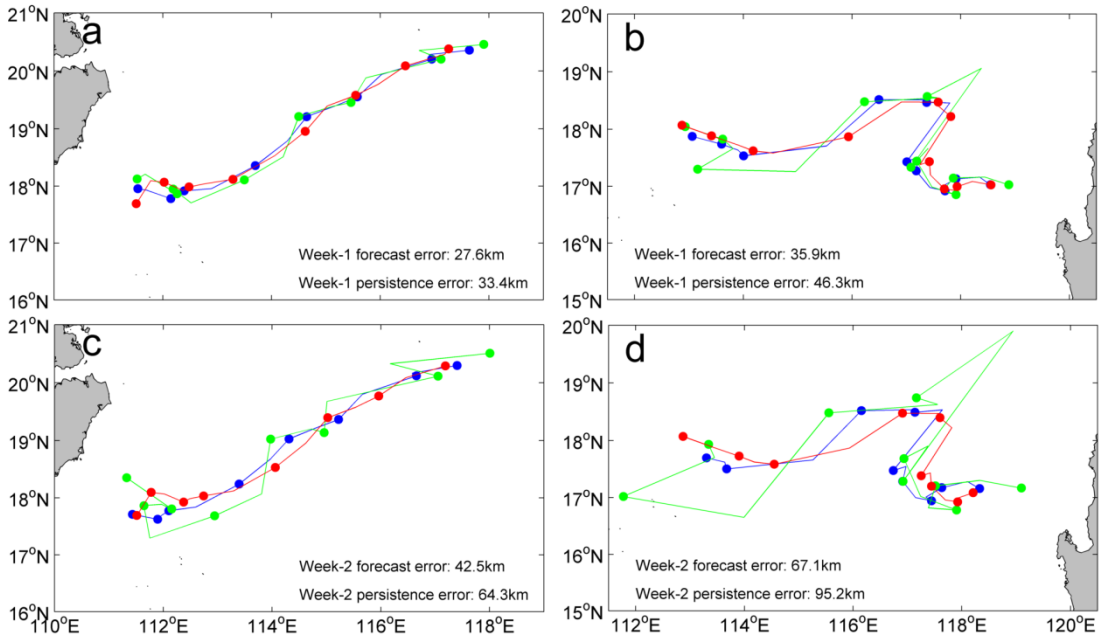

Figure 5. A comparison of the satellite observed trajectory (red), the predicted trajectory by our model (blue) and persistence trajectory (green) at (a) week-1, (c) week-2. (b), (d) are the same as (a) and (c), respectively, but for a recurved trajectory. The biweekly eddy positions on each trajectory are shown by the solid circles.

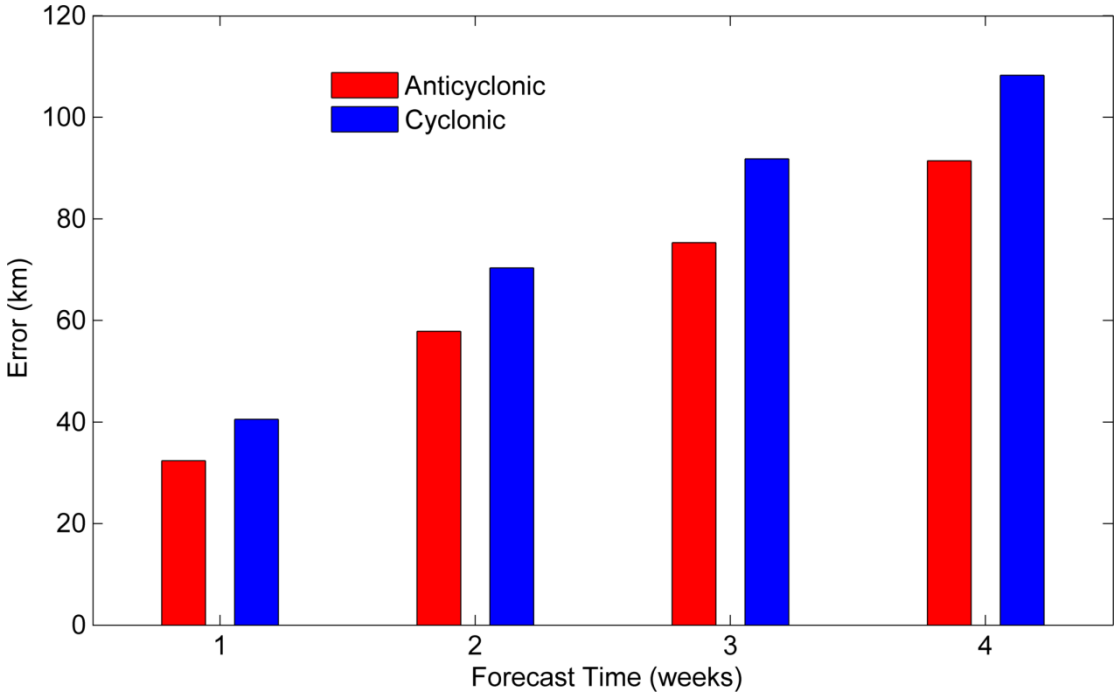

621

622 **Figure 6.** Comparison of the mean forecast errors between anticyclonic eddies (red)

623 and cyclonic eddies (blue) over a 4-week window.

624

625

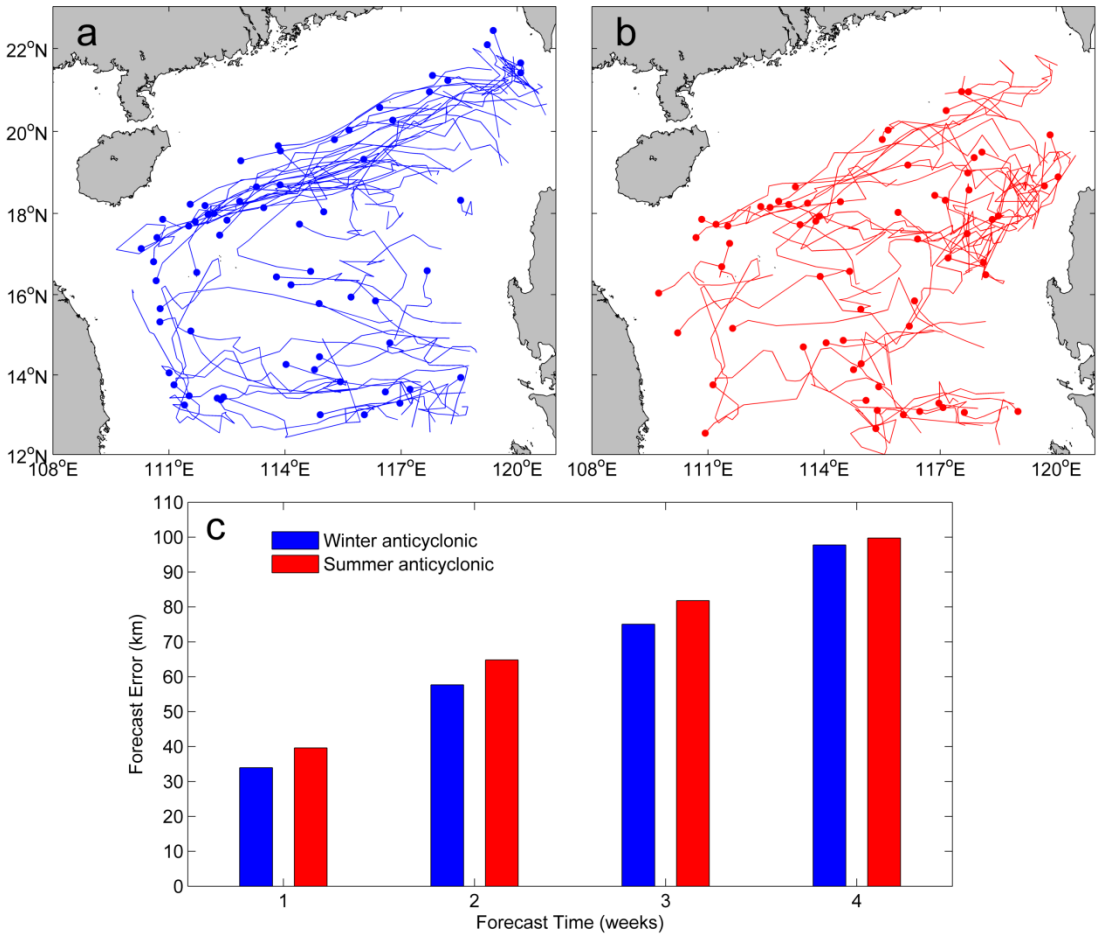

Figure 7. The trajectories of anticyclonic eddies in (a) winter and (b) summer with lifetime≥5 weeks in the northern South China Sea. The solid circle represents the ending position of each trajectory. (c) Comparison of their mean forecast errors over a 4-week window.

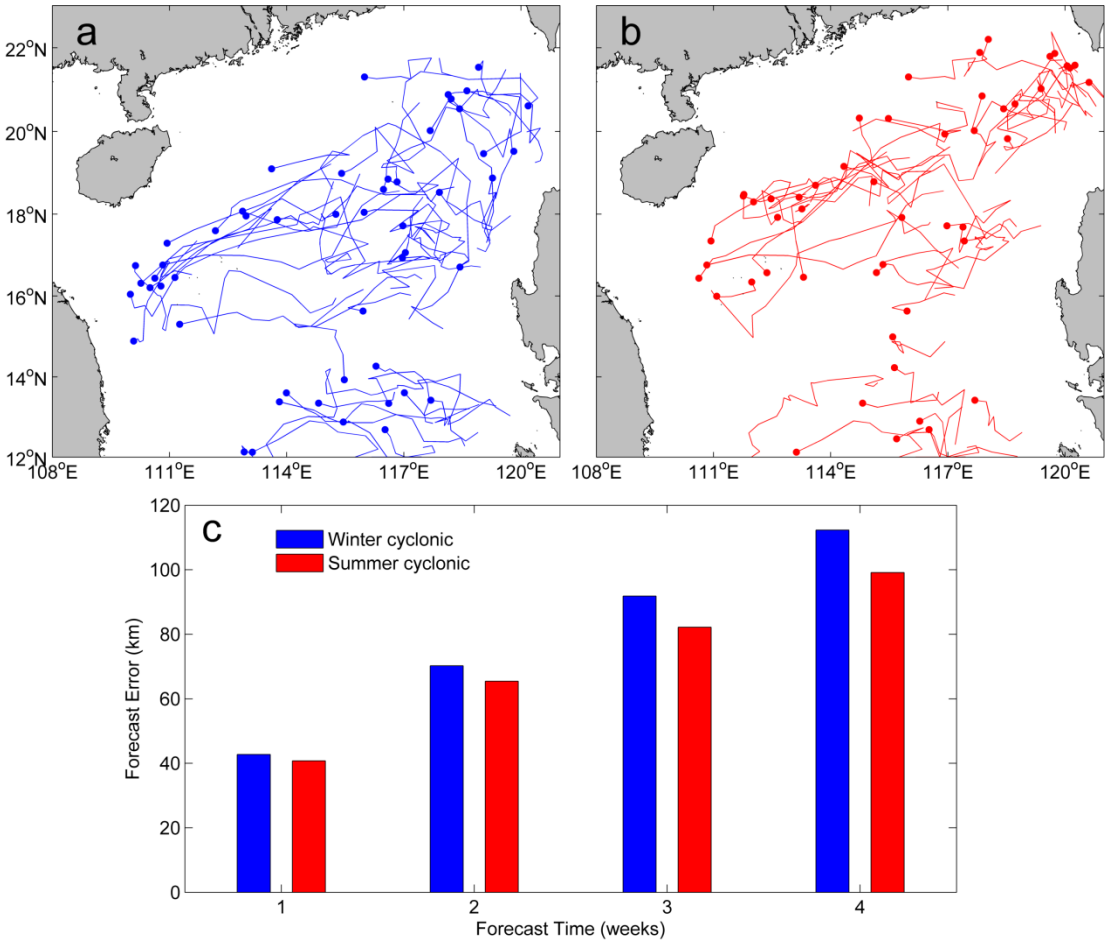

633

634

635 **Figure 8.** The same as Fig. 6, but for the cyclonic eddies.

636

637

638 **Table 1.** The eight predictands used in the predictive model

639

Predictand	Symbol
1-week zonal displacement	DX_1
1-week meridional displacement	DY_1
2-week zonal displacement	DX_2
2-week meridional displacement	DY_2
3-week zonal displacement	DX_3
3-week meridional displacement	DY_3
4-week zonal displacement	DX_4
4-week meridional displacement	DY_4

640

641

642 **Table 2.** The eight predictors used in the predictive model

643

Predictor	Symbol
Initial longitude (LON)	P_1
Initial latitude (LAT)	P_2
Eddy zonal motion past 1-week (U_PAST)	P_3
Eddy meridional motion past 1-week (V_PAST)	P_4
Climatological eddy zonal motion from MCC (U_CLIM)	P_5
Climatological eddy meridional motion from MCC (V_CLIM)	P_6
Initial zonal absolute geostrophic flow (U_ADT)	P_7
Initial meridional absolute geostrophic flow (V_ADT)	P_8

644

645 **Table 3.** Normalized regression coefficients $a_{i,j}$ ($b_{i,j}$) for use with the eddy zonal (meridional)

646 motion prediction equation

647

	j=1	j=2	j=3	j=4
i=1	-0.10 (0.03)	-0.14 (0.04)	-0.18 (0.05)	-0.24 (0.06)
i=2	0.10 (0.02)	0.13 (0.01)	0.16 (0.00)	0.18 (-0.03)
i=3	0.26 (0.00)	0.21 (0.03)	0.19 (0.07)	0.18 (0.09)
i=4	-0.02 (0.19)	-0.01 (0.10)	0.01 (0.08)	0.00 (0.08)
i=5	0.14 (0.09)	0.19 (0.13)	0.23 (0.16)	0.26 (0.16)
i=6	0.05 (0.17)	0.07 (0.23)	0.09 (0.26)	0.16 (0.27)
i=7	-0.05 (0.02)	-0.07 (0.02)	-0.07 (0.02)	-0.07 (0.03)
i=8	-0.03 (-0.07)	-0.01 (-0.08)	0.02 (-0.09)	0.04 (-0.09)

648

649

650 **Table 4.** Comparison of mean forecast distance errors (km) of the persistence, multiple linear
651 regression (MLR), and artificial neural network (ANN) method
652

Forecast weeks	Persistence	MLR	ANN
1	47.6	38.1	37.8
2	95.2	64.8	64.1
3	135.0	86.6	84.7
4	180.5	106.5	102.3

653 **Table 5.** Statistics of our multiple linear regression model for different forecast time of eddy propagation positions in terms of longitudes (latitudes)
654

Forecast weeks	Total/Predicted Number of Points	RMSE, km	Correlation Coefficient	Mean Distance Error, km
1	2604/623	32.7 (29.5)	0.99 (0.99)	38.1
2	2310/549	55.1 (47.3)	0.97 (0.98)	64.8
3	2016/475	72.5 (61.4)	0.95 (0.97)	86.6
4	1722/401	89.2 (73.5)	0.93 (0.95)	106.5

655 Note: the total/predicted number of points refers to the eddy positions at 7-day time interval in the whole/predicted eddy trajectories during 1992-2013/2009-2013;
656 the RMSE is the root mean square error between the predicted and the observed longitude (latitude).
657